Supplementary Information

Modulation of Cu and Rh single-atoms and nanoparticles for high-performance hydrogen evolution activity in acidic media

*Siraj Sultan,[†ab] Muhammad Hanif Diorizky,[†a] Miran Ha,[†ab] Jitendra N. Tiwari,[ab] Hansaem Choi,[b] Ngoc Kim Dang,[a] Pandiarajan Thangavel,[a] Jong Hoon Lee,[c] Hu Young Jeong,[c] Hyeon Suk Shin,[*a] Youngkook Kwon[* b] and Kwang S. Kim[*a]*

[a] Department of Chemistry, Ulsan National Institute of Science and Technology (UNIST), 50 UNIST-gil, Ulsan 44919, Republic of Korea.

[b] School of Energy & Chemical Engineering, Ulsan National University of Science and Technology (UNIST), Ulsan 44919, Republic of Korea.

[c] UNIST Central Research Facilities, UNIST, Ulsan, Republic of Korea.

[†]These authors contributed equally to this work.

*Correspondence and requests for materials should be addressed to H.S.K. (E-mail: shin@unist.ac.kr) or Y.K. (ykwon@unist.ac.kr) or K.S.K. (Email: kimks@unist.ac.kr).

Detection of the H_2 product and Faradaic efficiency

The H_2 product was quantitatively analyzed in real-time from the cathodic part of the H-cell reactor by an online gas chromatograph (GC, model iGC 7200A) equipped with a thermal conductivity detector (TCD for H_2 detection) and flame ionization detectors (FIDs for carbon product detection). High purity N_2 (99.9999%) was used as a carrier gas for chromatography. The GC spectra for the H_2 product were collected after each 40 min interval for 300 min. The actual amount of H_2 generated during the 5 h chronoamperometric test was calculated from the area of the GC spectrum using the H_2 calibration curve from the standard gases.

The Faradaic efficiency was calculated using the actual amounts of H_2 products obtained from GC divided by the theoretical amount of H_2 by using the following equation:

$$Faradaic\ Efficiency = \frac{Experiment\ amount\ of\ H_2\ produced}{Theoretical\ amount\ of\ H_2\ produced} * 100$$

The theoretical amount of H_2 gas was calculated using Faraday's law equation

$$n_{H_2} = \frac{I \times t}{z \times F}$$

where n is the number of mol, I is the current in ampere, t is the time in seconds, z is the electron transfer during the reaction (for H_2 z = 2), and F is the Faraday constant (96,485 C mol^{-1}).

Turnover Frequency

Turnover frequency (TOF) of Cu/Rh(SAs)+Cu_2Rh (NPs)/G_N was calculated using the equation:[1]

$$TOF = \frac{Number\ of\ H_2\ produced\ per\ geometric\ area}{Number\ of\ active\ sites\ per\ geometric\ area}$$

The number of H_2 molecules produced per geometric area can be calculated using the equation.

$$H_2 Turnover = j(mAcm^{-2}) \times \frac{1\ C\ s^{-1}}{1000\ mA} \times \frac{1\ mol\ e^-}{96485\ C} \times \frac{1}{z} \times N_A$$

where j is the current density (mA cm^{-2}), z is the number of electrons involved in the reaction (in case of HER, z = 2), and N_A is the Avogadro constant (6.02×10^{23}). Using current density at an overpotential of 20 mV, the H_2 turnover frequency for Cu/Rh(SAs)+Cu_2Rh (NPs)/G_N can be obtained as follows:

$$H_2\ turnover = 36.69\ mA\ cm^{-2} \times \frac{1\ C\ s^{-1}}{1000\ mA} \times \frac{1\ mol\ e^-}{96485\ C} \times \frac{1\ mol\ H_2}{2\ mol\ e^-} \times 6.022 \times 10^{23} \frac{H_2}{mol\ H_2}$$

$$= 1.145 \times 10^{17} H_2\ s^{-1} cm^{-2}$$

Meanwhile, the number of active sites was calculated by the equation:

$$Number\ of\ active\ sites = wt.\% \times loading\ amount \times \frac{1\ mmol}{MW} \times N_A\ sites\ mmol^{-1}$$

where wt.% is the weight of the metal in a catalyst (we use only the Rh content for TOF calculation), MW is the molecular weight, and N_A is Avogadro constant. The ICP-OES analysis gives the amount of Rh in Cu/Rh(SAs)+Cu_2Rh(NPs)/G_N as 5.55 wt%. So, the number of active sites was obtained as follows:

$$Number\ of\ active\ sites = \frac{5.55}{100} \times 0.285\ mg\ cm^{-2} \times \frac{1\ mmole}{102.9055\ mg} \times 6.022 \times 10^{20} sites\ mmol^{-1}$$

$$= 9.256 \times 10^{16} sites\ cm^{-2}$$

Giving TOF value for Cu/Rh(SAs)+Cu_2Rh(NPs)/G_N is:

$$TOF = \frac{1.145 \times 10^{17} H_2\ s^{-1} cm^{-2}}{9.256 \times 10^{16} sites\ cm^{-2}} = 1.237\ H_2\ sites^{-1}\ s^{-1}$$

Using a similar method, the TOF value of catalyst **5** and commercial Pt-C catalyst was calculated to be 0.0378 H_2 $sites^{-1}$ s^{-1} and 0.329 H_2 $sites^{-1}$ s^{-1}, respectively.

Core level XPS spectra of catalysts 1-6, Cu(SAs) + Cu(NPs)/G_N, Cu(SAs)/G_N and Cu/Rh(SAs) + Cu_2Rh(NPs)/G

Figs. S14-22 show the core level XPS spectra of Rh 3d, Cu 2p and N 1s of catalysts **1-6**, Cu(SAs)+Cu(NPs)/G_N, Cu(SAs)/G_N and Cu/Rh(SAs)+Cu_2Rh(NPs)/G. In catalysts **1-6,** the splitting pattern of Rh $3d_{5/2}$ and Rh $3d_{3/2}$ spectra shows two main dominant peaks of zero valence Rh atom at binding energies of 307.25-307.51eV and 312.00-312.14 eV and two minor peaks of ionic species at binding energies of (308.10-309.54 eV and 313.00-313.61 eV)[2] (**Figs. S14a-S19a**). Similarly, the core level XPS spectra of Cu 2p in **1-4,** Cu(SAs)+Cu(NPs)/G_N and Cu(SAs)/G_N show two main sharp and strong peaks of metallic Cu at binding energies of 932.29-932.74 eV and 952.04-952-63 eV and two small peaks of ionic species at binding energies of 934.56-934.91 eV and 954.12-955.65 eV with shakeup satellite peaks at 940.75-941.77 eV and 943.68-944.45 eV (**Figs. S14b-S17b and S20a and 21a**). The binding energies of N 1s core-level XPS spectra (398.33-398.54 eV, 399.55-399.78 eV and 400.28-401.09 eV) show that the nitrogen in catalysts [**1-5,** Rh(SAs)/G_N , Cu(SAs)+Cu(NPs)/G_N and Cu(SAs)/G_N] are present in the form of pyridinic-N, metal-N and graphitic-N[1,3] (**Figs. S14c-S17c, S18b-S21b**). The XPS analysis of Cu/Rh(SAs)+Cu_2Rh(NPs)/G catalyst shows the core-level XPS spectra of Rh and Cu, but not the spectra of N (**Fig S22)**. In Cu/Rh(SAs)+Cu_2Rh(NPs)/G, the splitting pattern of Rh $3d_{5/2}$ and Rh$3d_{3/2}$ spectra in Cu/Rh(SAs)+Cu_2Rh(NPs)/G shows two main dominant peaks of zero valence Rh atom at binding energies of 307.32 and 312.08 eV and two minor peaks of ionic species at binding energies of 308.21 and 313.07 eV. The Rh $3d_{3/2}$ spectra in this Cu/Rh(SAs)+Cu_2Rh(NPs)/G catalyst also shows a peak at 309.63 eV which corresponded to the surface oxidized Rh species [4](Fig S22a). Similarly, the core-level XPS spectrum of Cu 2P shows two main sharp and strong peaks of metallic Cu at binding energies of 932.56 and 952.31 eV and

two small peaks of ionic species at binding energies of 934.64 and 954.28 eV with shakeup satellite peaks at 941.99 and 943.88 eV (Fig S22b). The core-level XPS spectrum of N 1s does not show any peak indicating that the Cu/Rh(SAs)+Cu_2Rh(NPs) is supported on graphene but not on the N-doped graphene (Fig S22c).

Double-Layer Capacitance

Double-layer capacitance (C_{dl}) experiments were carried out by cycling the potential in a non-Faradaic region (75 – 115 mV v.s. RHE) with different applied scan rates of 5, 10, 15, 20 and 25 mV s^{-1} in an H_2-saturated 0.5 M H_2SO_4 solution. The current from the cyclic voltammetry curves at a potential of 100 mV was plotted versus the applied scan rate and the slope from their linear plot was assigned to C_{dl}.

Calibration of Reference Electrode

Before each electrochemical experiment, the reference electrode was calibrated by a three-electrode setup with a saturated calomel electrode (SCE) as the reference electrode and Pt wire as both working and counter electrodes. The calibration was performed in the high purity hydrogen saturated 0.5 M H_2SO_4 electrolytes. Linear-sweep voltammetry (LSV) was performed at a scan rate of 1 mV s^{-1} and the potential that crossed 0 mA was taken as thermodynamic potential (vs. SCE) for the hydrogen electrode (**Fig. S33**).

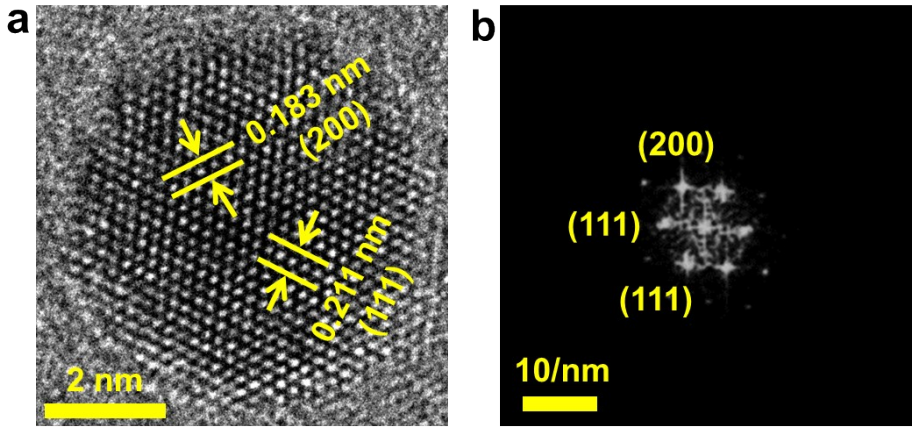

Fig. S1 HRTEM image of single Cu_2Rh (NP) and their corresponding FFT pattern in **1**: Cu/Rh(SAs)+Cu_2Rh(NPs)/G_N. **(a)** HR TEM image, **(b)** FFT image.

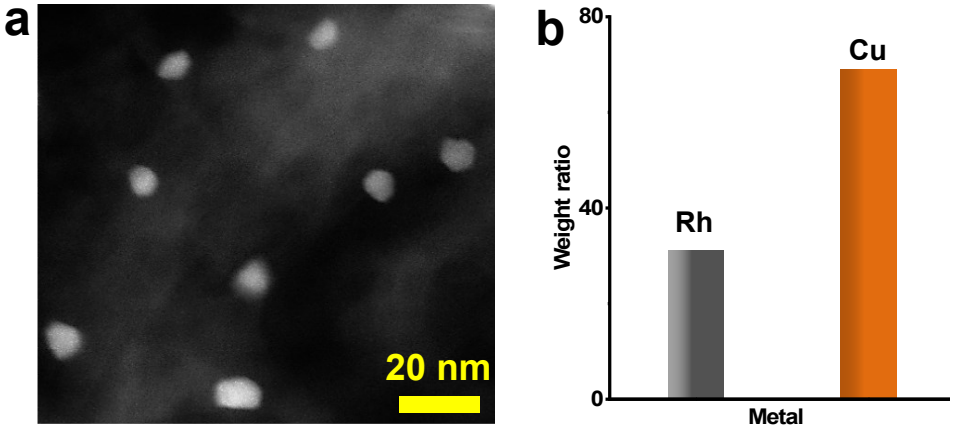

Fig. S2 TEM-EDX weight ratio composition of Rh and Cu in **1**: Cu/Rh(SAs)+Cu_2Rh(NPs)/G_N. **(a)** HAADF–STEM image, **(b)** corresponding Rh and Cu weight ratio.

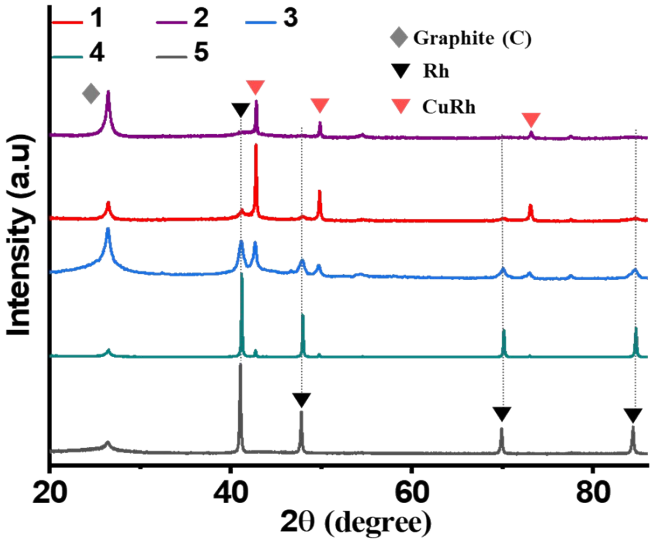

Fig. S3 XRD spectra for catalysts **1-5**. The XRD pattern of **5** shows the diffraction peaks at position 2Θ of 41.06°, 47.79°, 69.90°, 84.39°, corresponding respectively to (111), (200), (220), and (311) planes of cubic Rh crystal structure (JCPDS#01-089-7383). In XRD patterns of **1-4**, the peaks related to the cubic Rh crystalline structure weakened or vanished in favor of new diffraction peaks at 42.77°, 49.78°, 73.04°, and 88.54° that can be assigned respectively to (111), (200), (220) and (311) lattices of RhCu crystal (JCPDS#03-065-9051). The intensity of new evolved peaks grew in intensity with increasing the amount of Cu. [**1:** Cu/Rh(SAs)+Cu_2Rh(NPs)/G_N, **2**: Cu/Rh (SAs)+Cu_3Rh(NPs)/G_N, **3**: Cu/Rh(SAs)+CuRh(NPs)/G_N, **4**: Cu/Rh(SAs)+$CuRh_5$(NPs)/G_N, **5**: Rh(SAs)+Rh(NPs)/G_N].

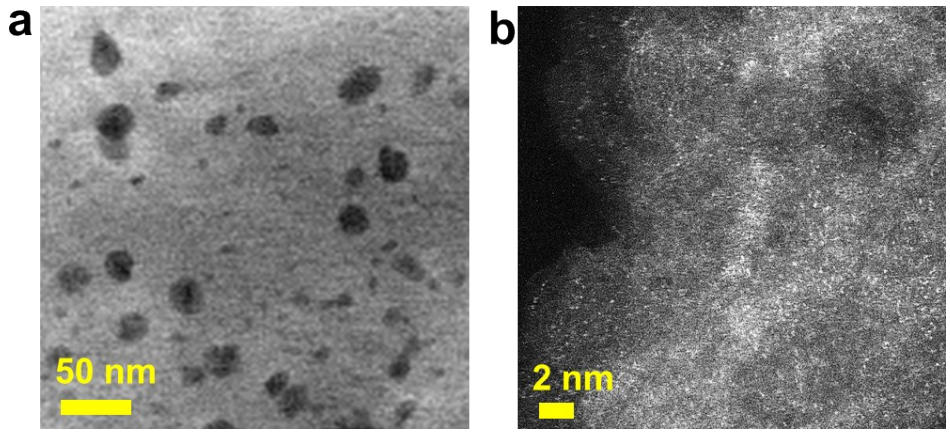

Fig. S4 TEM image and HAADF–STEM image for **(a)** Cu_3Rh (NPs), **(b)** Cu/Rh (SAs) in catalyst **2**: Cu/Rh(SAs)+Cu_3Rh(NPs)/G_N.

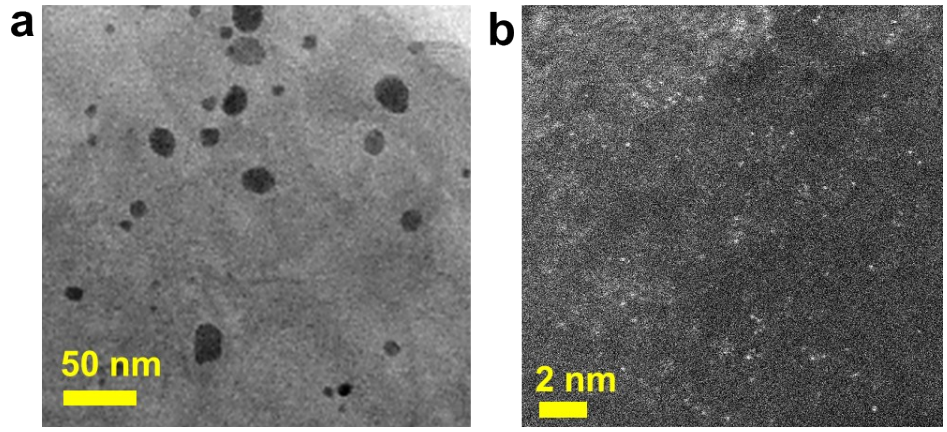

Fig. S5 TEM image and HAADF–STEM image for **(a)** CuRh(NPs) **(b)** Cu/Rh(SAs) in catalyst **3**: Cu/Rh(SAs)+CuRh(NPs)/G_N.

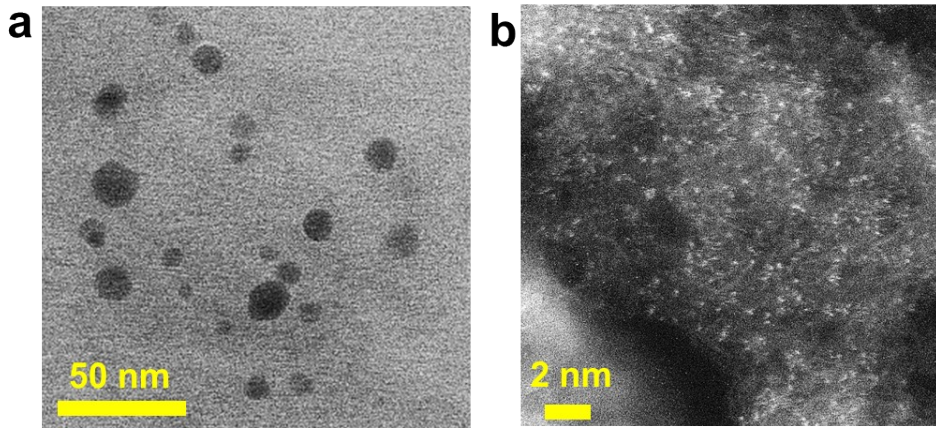

Fig. S6 TEM image and HAADF–STEM image for **(a)** $CuRh_5$(NPs), **(b)** Cu/Rh(SAs) in catalyst **4**: Cu/Rh(SAs)+$CuRh_5$(NPs)/G_N.

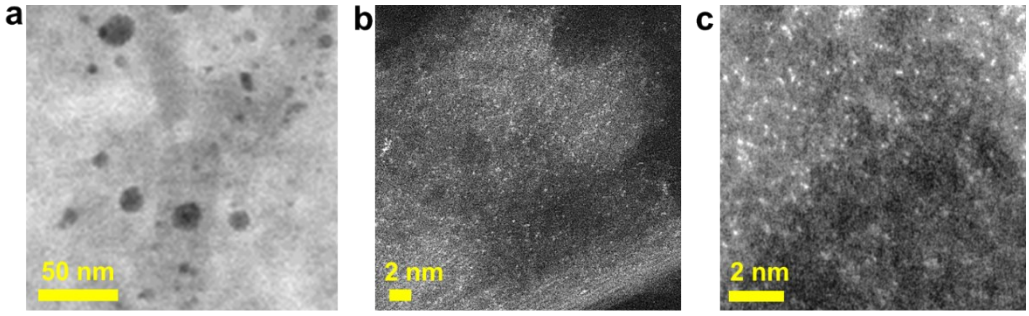

Fig. S7 TEM image and HAADF–STEM image for **(a)** Rh(NPs), **(b, c)** Rh(SAs) in catalyst **5**: Rh(SAs) Rh(NPs)/G_N.

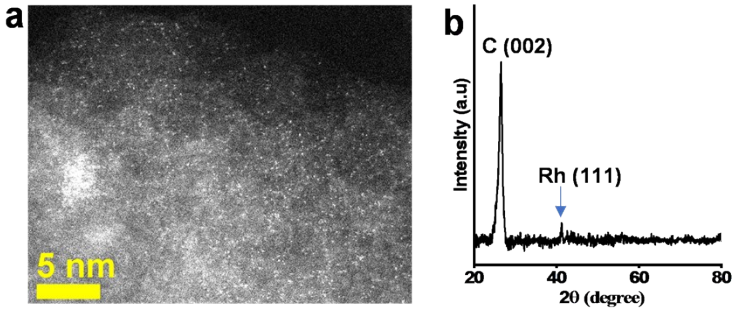

Fig. S8 HAADF–STEM image and XRD pattern of catalyst **6**. **(a)** HAADF–STEM image, **(b)** XRD pattern showing a main dominant peak at 26.4°, which correspond to the planes (002) of graphitic carbon and a small peak of Rh (111) at ~41.1°. This indicates that the catalyst contains the majority of Rh(SAs) and a few small sizes Rh(NPs) on the G_N surface.

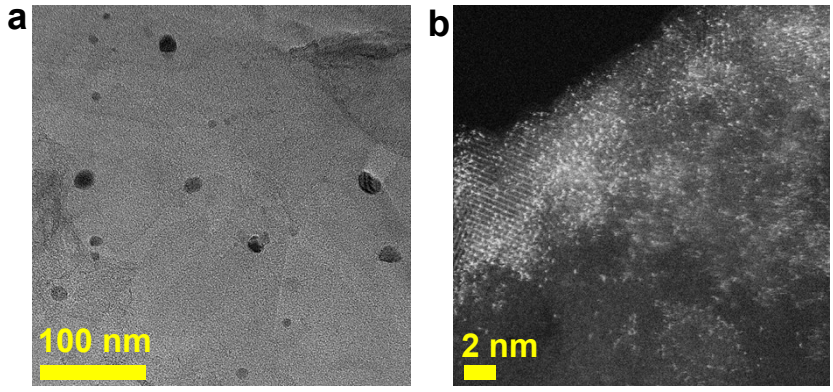

Fig. S9 TEM image and HAADF–STEM image for **(a)** CuRh(NPs) **(b)** Cu/Rh(SAs) in Cu/Rh(SAs)+Cu_2Rh(NPs)/G.

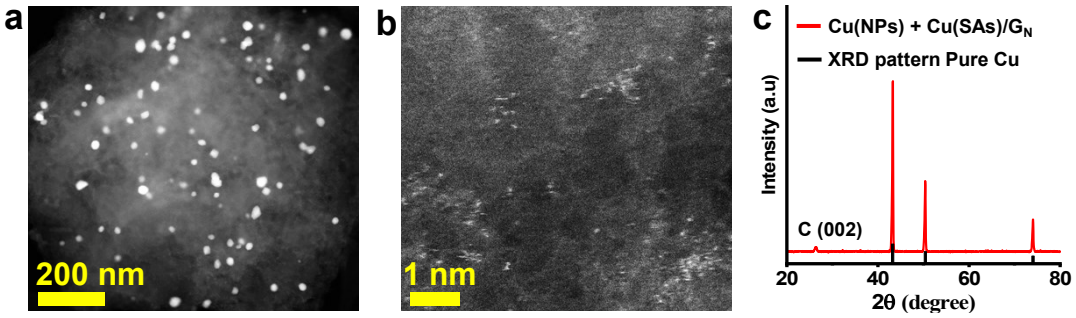

Fig. S10 HAADF–STEM images and XRD pattern of Cu(NPs)+Cu(SAs)/G_N. **(a)** Cu(NPs), **(b)** Cu(SAs), **(c)** The XRD pattern of Cu(NPs)+Cu(SAs)/G_N showing the diffraction peaks at position 2Θ of 43.29°, 50.43° and 74.13°, corresponding respectively to (111), (200) and (220), and (311) planes of the cubic Cu crystal structure (JCPDS# 00-004-0836).

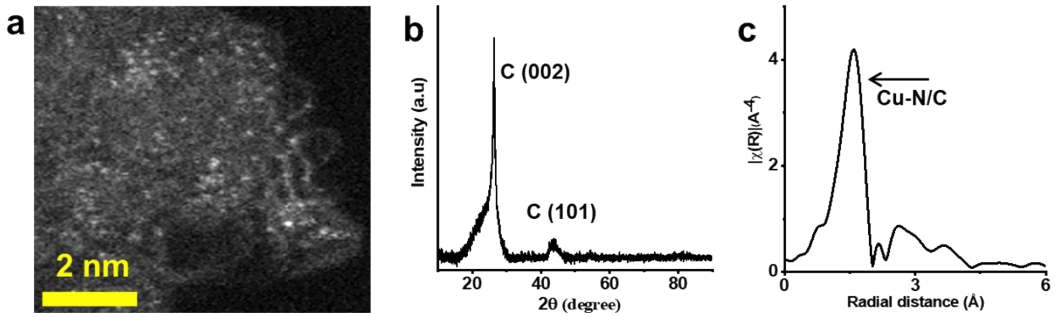

Fig. S11 HAADF-STEM, XRD and FT-EXAFS characterization of Cu(SAs)/G_N. **(a)** HAADF–STEM image, **(b)** XRD pattern shows a main dominant peak at 26.4° and another small peak at 44.4°, which correspond to the planes (002) and (101), respectively, of graphitic carbon (JCPDS#00-012-0212). No peaks of Cu crystals were detected. **(c)** FT-EXAFS of Cu at the K-edge shows the main coordination of Cu-N/C sites.

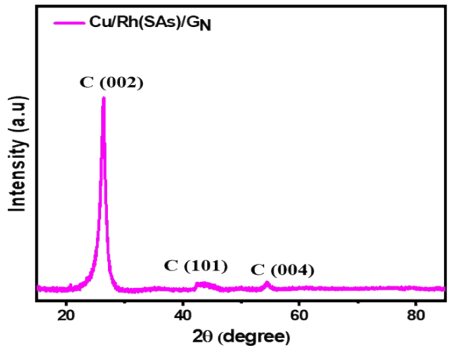

Fig. S12 XRD pattern of Cu/Rh(SAs)/G_N shows a main dominant peak at 26.4° and another small peak at 43.1° and 54.4°, which correspond to the planes (002), (101) and (004), respectively, of graphitic carbon (JCPDS#00-008-0415). No peaks of Cu and Rh crystals were detected, which indicates that the majority of Rh and Cu are distributed as SAs on the G_N surface.

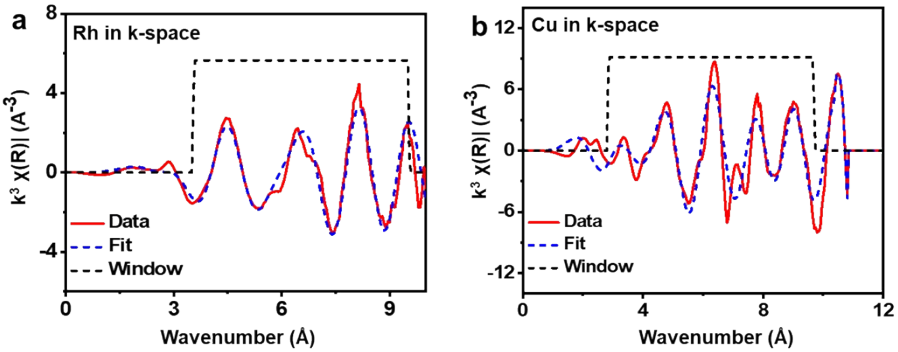

Fig. S13 The corresponding EXAFS $\chi(k)$ signals in k-space and fitted curves for Rh and Cu in **1**: Cu/Rh(SAs)+Cu_2Rh(NPs)/G_N. **(a)** Rh, **(b)** Cu.

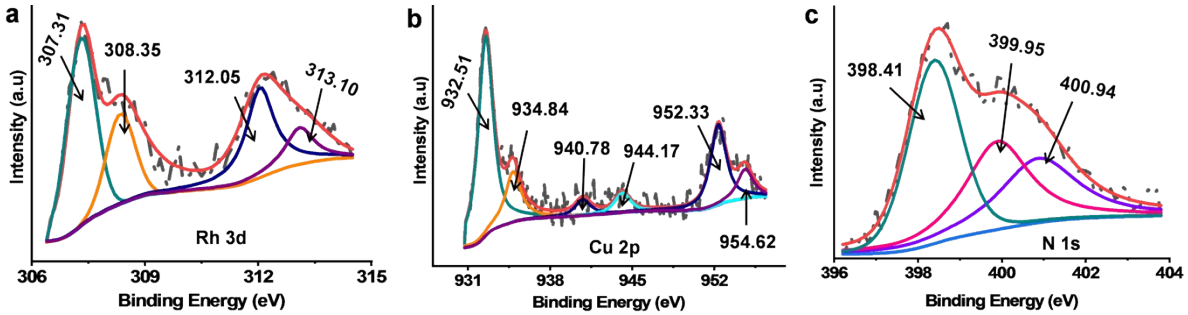

Fig. S14 XPS core-level spectra of **1**: Cu/Rh(SAs)+Cu_2Rh(NPs)/G_N. **(a)** Rh 3d, **(b)** Cu 2p, **(c)** N 1s.

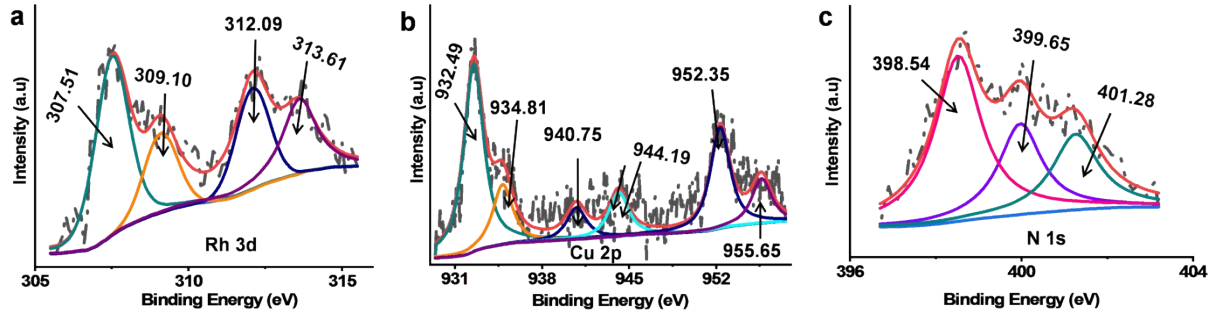

Fig. S15 XPS core-level spectra of **2**: Cu/Rh(SAs)+Cu_3Rh(NPs)/G_N. **(a)** Rh 3d **(b)** Cu 2p **(c)** N 1s.

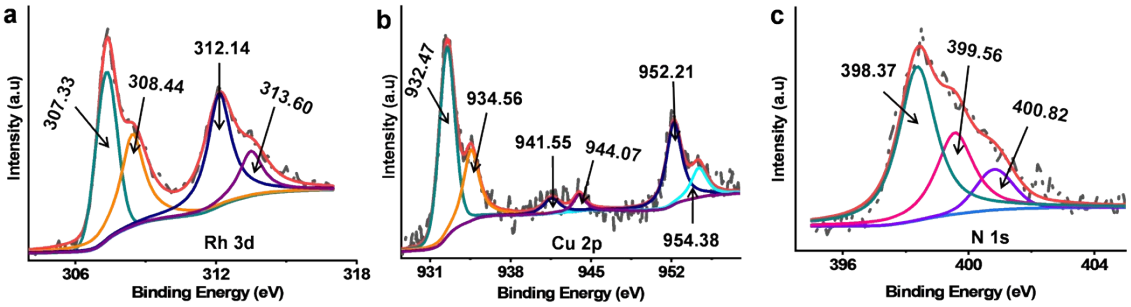

Fig. S16 XPS core-level spectra of **3**: Cu/Rh(SAs)+CuRh(NPs)/G_N. **(a)** Rh 3d, **(b)** Cu 2p, **(c)** N 1s.

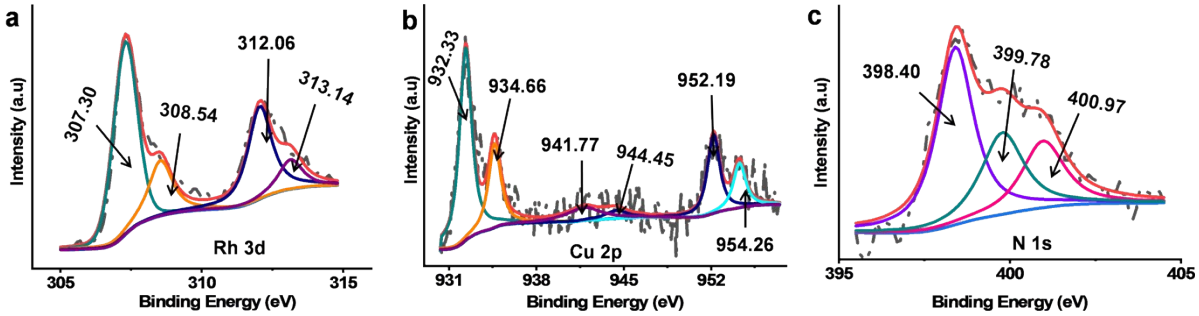

Fig. S17 XPS core-level spectra of **4**: Cu/Rh(SAs)+$CuRh_5$(NPs)/G_N. **(a)** Rh 3d, **(b)** Cu 2p **(c)** N 1s.

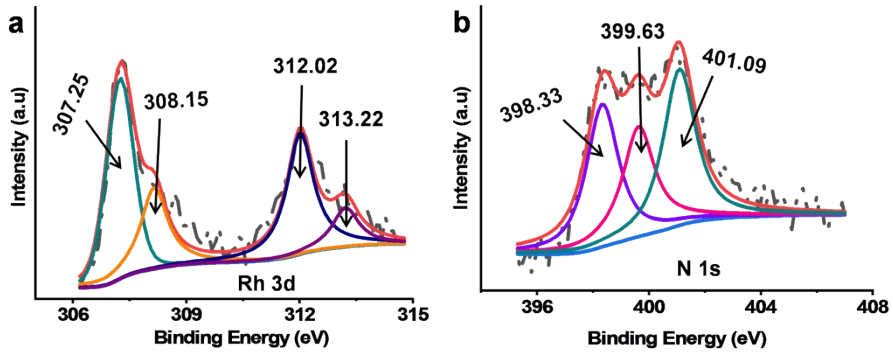

Fig. S18 XPS core-level spectra of **5**: Rh(SAs)+Rh(NPs)/G_N. **(a)** Rh 3d, **(b)** N 1s.

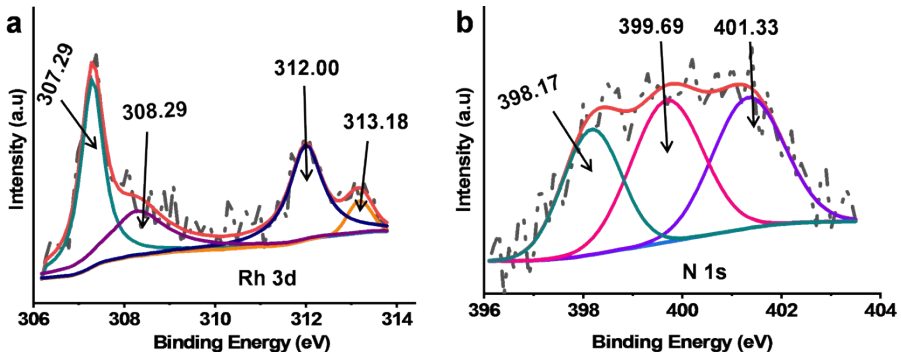

Fig. S19 XPS core-level spectra of **6**: Rh(SAs)/G_N. (a) Rh 3d, (b) N 1s.

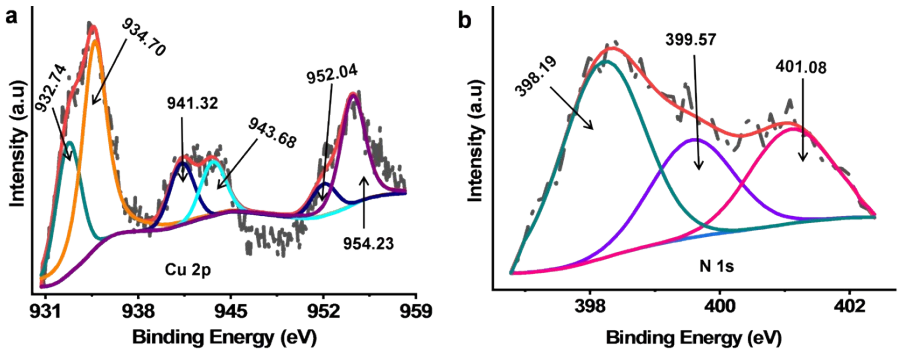

Fig. S20 XPS core-level spectra of Cu(SAs)+Cu(NPs)/G_N. (a) Cu 2p, (b) N 1s.

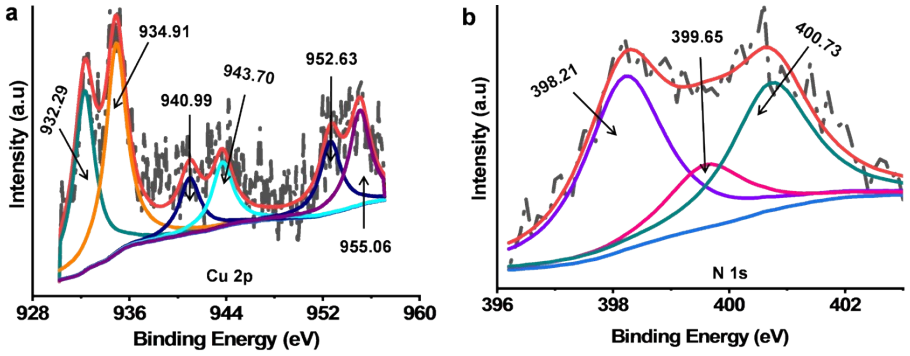

Fig. S21 XPS core-level spectra of Cu(SAs)G_N. **(a)** Cu 2p, **(b)** N 1s.

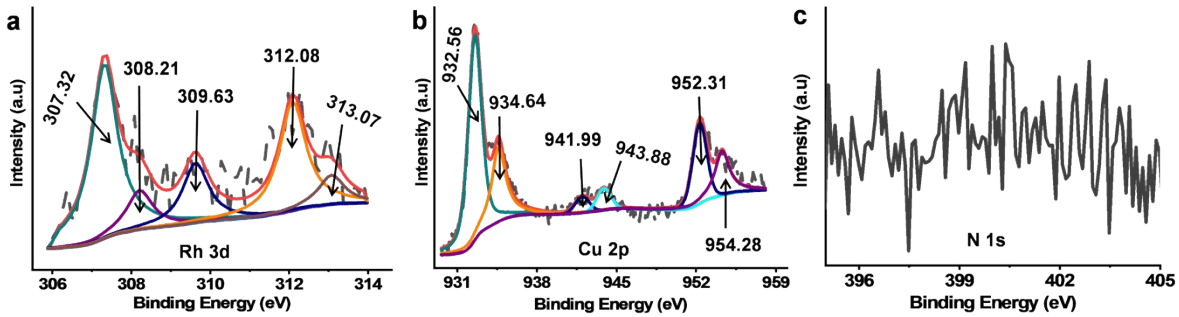

Fig. S22 XPS core-level spectra of Cu/Rh(SAs)+Cu_2Rh(NPs)/G. **(a)** Rh 3d, **(b)** Cu 2p, **(c)** N 1s. The core-level XPS spectra of N 1s does not show any peaks indicating that the Cu/Rh(SAs)+Cu_2Rh(NPs)/G contains only graphene surface but not N-doped graphene.

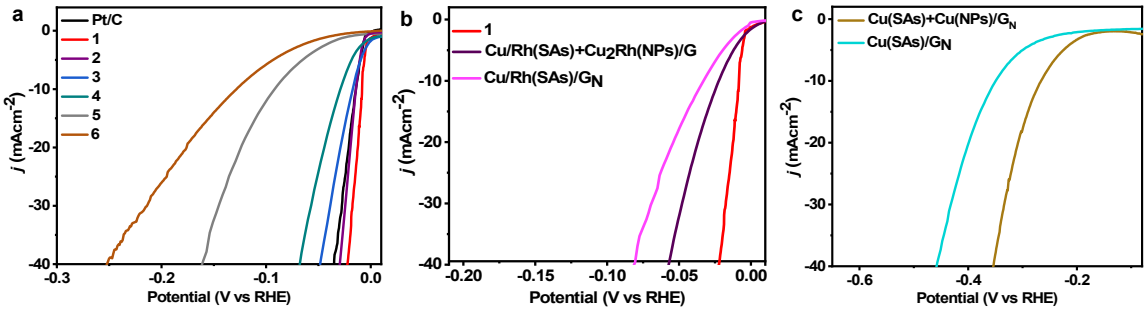

Fig. S23 Electrocatalytic performance in H_2-saturated 0.5 M H_2SO_4 at a scan rate of 2 mV s^{-1}. **(a)** HER polarization curves of **1-5,** Rh(SAs)/G_N and Pt/C. **(b)** HER polarization curve of **1**, Cu/Rh(SAs)+Cu_2Rh(NPs)/G and Cu/Rh(SAs)/G_N. **(c)** HER polarization curves of Cu(SAs)/G_N + Cu(NPs) and Cu(SAs)/G_N. [**1**: Cu/Rh(SAs)+Cu_2Rh(NPs)/G_N, **2**: Cu/Rh (SAs)+Cu_3Rh (NPs)/G_N, **3**: Cu/Rh(SAs)+CuRh(NPs)/G_N, **4**: Cu/Rh(SAs)+$CuRh_5$(NPs)/G_N, **5**: Rh(SAs)+Rh (NPs)/G_N, **6:** Rh(SAs) /G_N]. Note: In the Cu/Rh(SAs)+Cu_2Rh(NPs)/G catalyst, SAs and NPs are supported on the graphene surface but not on nitrogen-doped graphene.

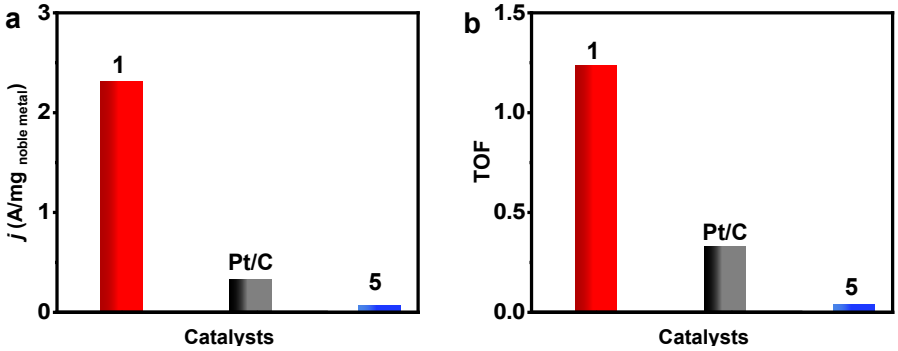

Fig. S24 Mass activity and turnover frequency (TOF) at an overpotential of 20 mV for the catalysts **1**, **5** and Pt/C. (a) Mass activity. (b) TOF. [**1**: Cu/Rh(SAs)+Cu_2Rh(NPs)/G_N, **5**: Rh(SAs)+Rh (NPs)/G_N]

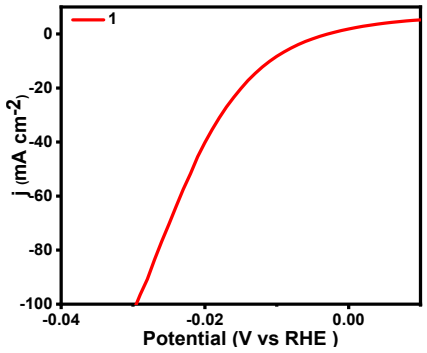

Fig. S25 HER polarization curves of catalyst **1** on Toray carbon paper [**1**: Cu/Rh(SAs)+Cu_2Rh(NPs)/G_N].

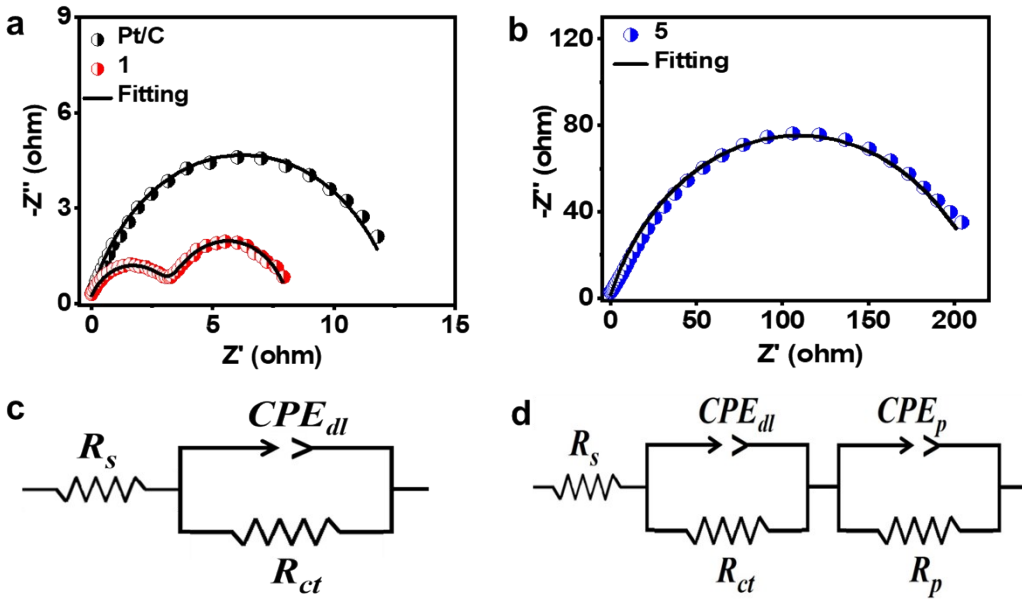

Fig. S26 Electrochemical impedance spectra and data fitting of **(a)** catalyst **1**, Pt/C **(b)** catalyst **5**; and **(c, d)** corresponding equivalent electrical circuit. **(c)** was used for fitting spectra of Pt/C and catalyst **5** which consists of R_s = solution resistance, R_{ct} = charge transfer resistance and CPE_{dl} = constant phase element related to double-layer. **(d)** was used for fitting spectra of catalyst **1** which consists of R_s, R_{ct}, CPE_{dl}, R_p = adsorption resistance related to the highly porous surface geometry of the catalyst and CPE_p = constant phase element related to the porosity of the material. The EIS spectra are consistent with the BET surface area: catalyst **1** shows a significantly higher surface area (**Fig. S27**) and pore volume (**Table S5**) compared to catalyst **5.** Therefore, the EIS Spectrum of catalyst **1** shows two repressed semi-circles; one semicircle represents the resistance related to the porosity of the materials on a high-frequency region (R_p), while the second semicircle on low-frequency region corresponds to the charge transfer resistance. [**1**: Cu/Rh(SAs)+Cu_2Rh(NPs)/G_N, **5**: Rh(SAs)+Rh(NPs)/G_N].

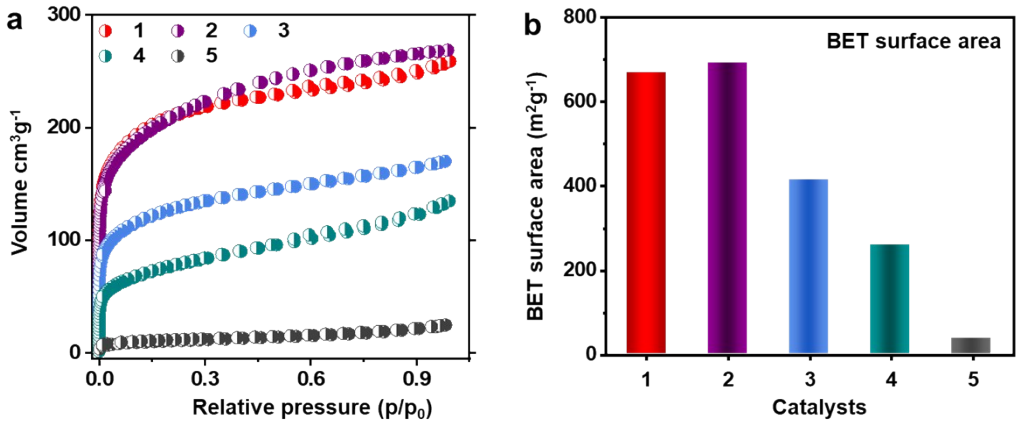

Fig. S27 Brunnauer-Emmett-Teller (BET) surface area of **1-5**. (a) Nitrogen adsorption–desorption isotherms, **(b)** corresponding BET surface area. [**1**: Cu/Rh(SAs)+Cu_2Rh(NPs)/G_N, **2**: Cu/Rh (SAs)+Cu_3Rh (NPs)/G_N, **3**: Cu/Rh(SAs)+CuRh(NPs)/G_N, **4**: Cu/Rh(SAs)+$CuRh_5$(NPs)/G_N, **5**: Rh(SAs)+Rh(NPs)/G_N].

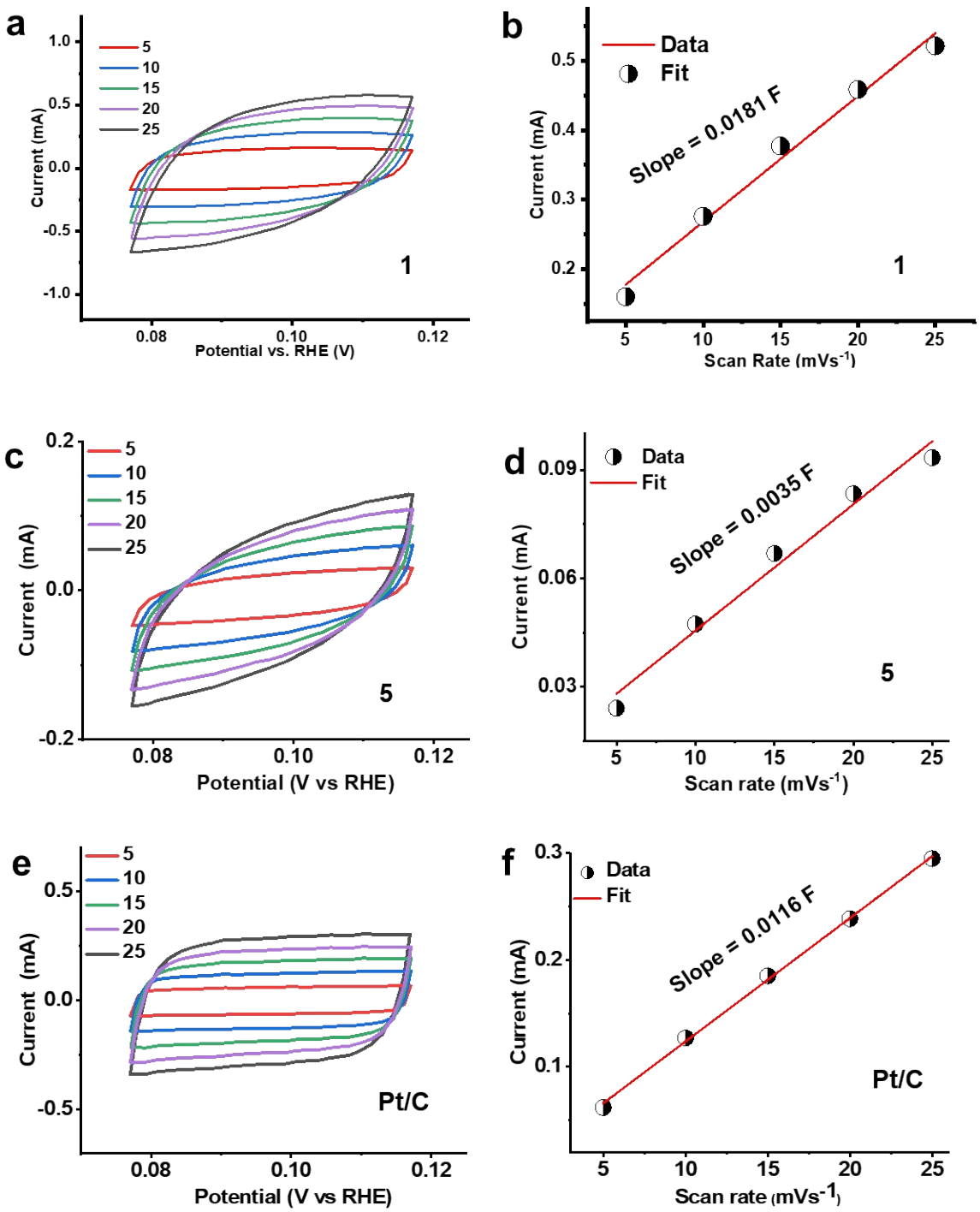

Fig. S28 Double-layer capacitance (C_{dl}) measurements from cyclic voltammetry in 0.5 M H_2-saturated 0.5 M H_2SO_4. **(a, c, e)** Cyclic voltammograms of **1, 5** and Pt/C recorded in a non-faradaic region at scan rates of 5-25 mV/s, **(b, d, f)** corresponding anodic capacitance currents vs scan rate at the potential of 100 mV vs RHE. [**1**: Cu/Rh(SAs)+Cu_2Rh(NPs)/G_N, **5**: Rh(SAs)+Rh(NPs)/G_N].

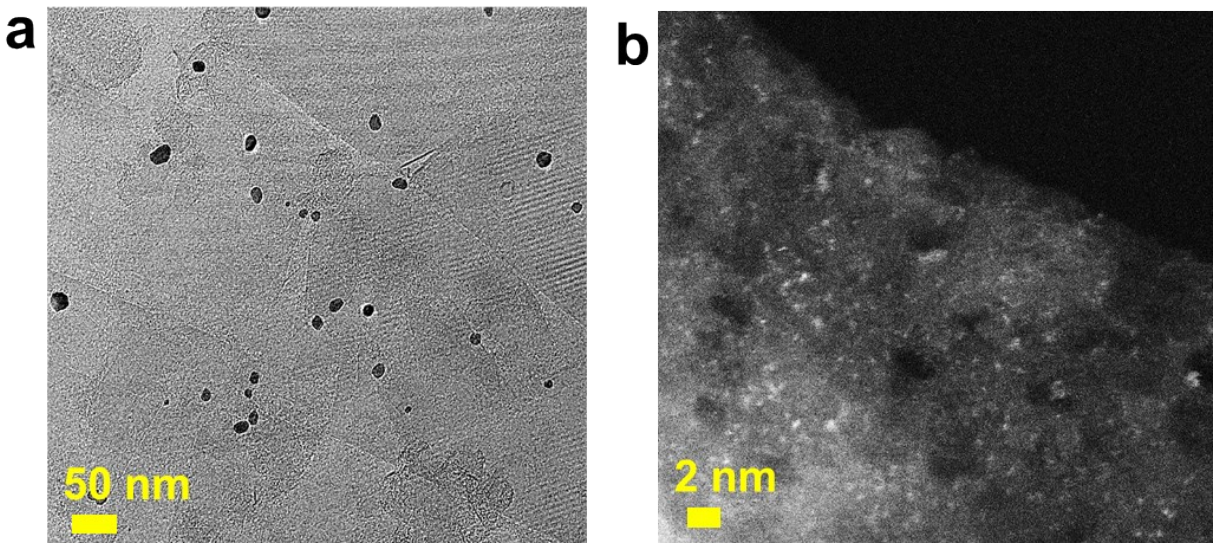

Fig. S29 TEM image and HAADF–STEM images of **1**: Cu/Rh(SAs)+Cu_2Rh(NPs)/G_N after 500h stability test. **(a)** TEM image. **(b)** HAADF–STEM image

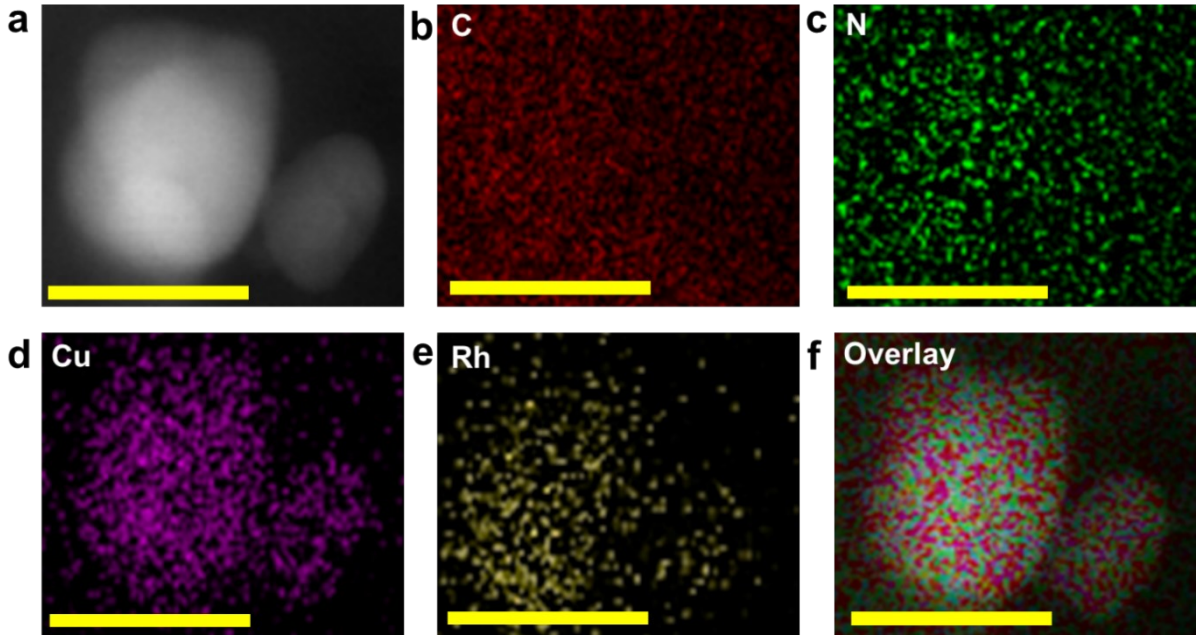

Fig. S30 HAADF–STEM image of Cu_2Rh(NP) and the corresponding individual element maps of C, N, Cu, and Rh and the overlay of Cu+Rh of **1**: Cu/Rh(SAs)+Cu_2Rh(NPs)/G_N after 500h stability test.

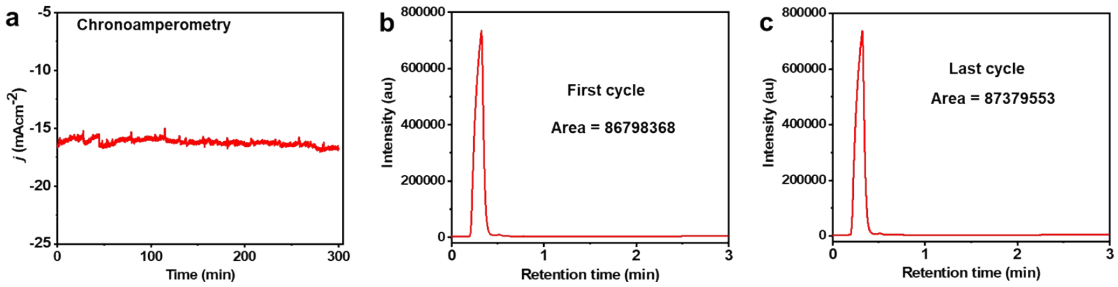

Fig. S31 Chronoamperometry and Gas chromatography (GC) measurements of **1**: Cu/Rh(SAs)+Cu_2Rh(NPs)/G_N (a) Chronoamperometry test for 300 min. (b) First cycle GC spectrum for the H_2 product recorded during the initial 40 minutes of the chronoamperometry test. (c) Last cycle GC spectrum for the H_2 product recorded at the last 300 minutes of the chronoamperometry test. Note: GC spectra for the H_2 product were collected after each 40 min interval for 300 min.

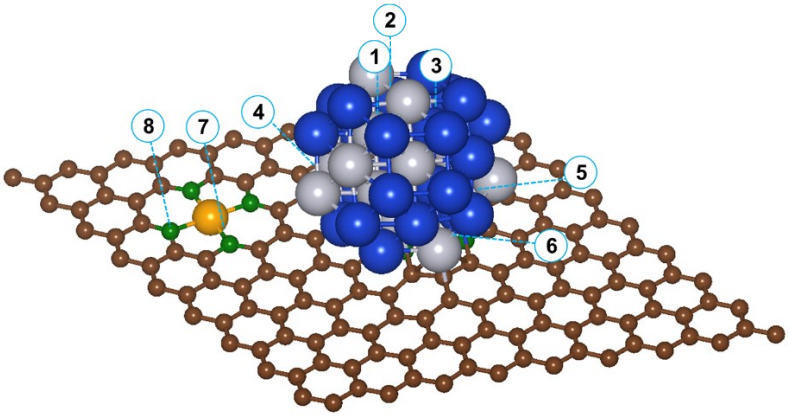

H adsorption Site	ΔG_{H^*} (eV)
1 (CuRh fcc)	0.03
2	-0.32
3	-0.17
4	-0.31
5	-0.24
6	-0.16
7 (Rh-N_4)	-0.08
8 (Cu-N_4)	1.30

Fig. S32 Gibbs free energies of hydrogen adsorption (ΔG_{H^*}) on various sites of Cu_2Rh_1-NPs/G_N and metal single-atom sites (Cu-N_4 and Rh-N_4) near Cu_2Rh_1-NP. The CuRh fcc site on Cu_2Rh_1 NP shows high activity for HER similar to balanced sites on Cu_2Rh_1 (111). Also, the Ru-N4 site near Cu_2Rh_1 is still active for the HER.

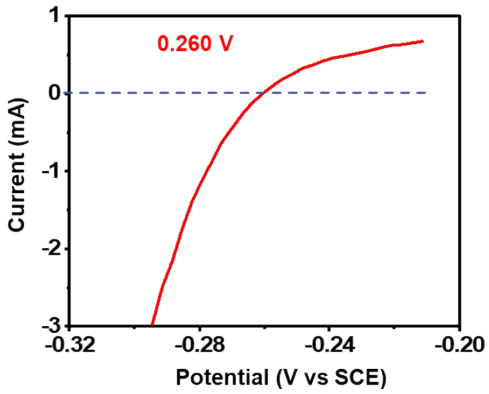

Fig. S33 Calibration of the reference electrode. Potential calibration curve for SCE reference electrode in H_2-saturated 0.5 M H_2SO_4. $E_{RHE} = E_{SCE} + 0.260$ V.

Table S1 Experimental weight ratio of $CuSO_4.5H_2O$ and $RhCl_3.xH_2O$ with graphene oxide (0.1g) and melamine (0.5g) used in the synthesis of catalysts.

Catalysts	**$CuSO_4.5H_2O$ (g)**	**$RhCl_3.xH_2O$ (g)**
1	0.2	0.05
2	0.22	0.038
3	0.15	0.07
4	0.1	0.10
5	00	0.10
6	00	0.035
Cu(SAs)Cu(NPs)/G_N	0.60	00
Cu(NPs)/G_N	0.2	00

Table S2 ICP-OES chemical composition (wt.%) analysis of Cu and Rh in catalysts **1-5**.

Catalysts	Cu	Rh	Cu: Rh	Composition
1	10.49	5.55	1.90: 1.00	Cu_2Rh
2	6.35	2.42	2.62: 1.00	$Cu_{2.6}Rh$ denoted Cu_3Rh
3	7.80	8.22	1.00: 1.05	CuRh
4	6.00	1.28	4.70: 1.00	$CuRh_{4.7}$ denoted $CuRh_5$
5	00	4.92	00: Rh	Rh

Table S3 Curve-fitting analysis for Rh K-edge EXAFS of 1: Cu/Rh(SAs)+Cu_2Rh(NPs)/G_N. Rh K-edge EXAFS curve fitting parameters (R: Bond distance, CN: Coordination number, σ^2: Debye-Waller factor, ΔE_0: energy shift).

R-factor:	**0.0014**			
Path	**R (Å)**	**CN (atoms)**	**σ^2 (Å)**	**ΔE (eV)**
Rh-C/N	2.11 ± 0.02	2	0.010 ± 0.002	-1.99 ± 2.81
Rh-C/N	2.13 ± 0.02	2	0.010 ± 0.002	-1.99 ± 2.81
Rh-C	2.58 ± 0.02	4	0.005 ± 0.001	-1.99 ± 2.81
Rh-Rh/Cu	2.69 ± 0.02	1.3	0.005 ± 0.001	-1.99 ± 2.81

Table S4 Curve-fitting analysis for Cu K-edge EXAFS of **1**: Cu/Rh(SAs)+Cu_2Rh(NPs)/G_N. Cu K-edge EXAFS curve fitting parameters (R: Bond distance, CN: Coordination number, σ^2: Debye-Waller factor, ΔE_0: energy shift).

R-factor:	**0.0092**			
Path	**R (Å)**	**CN (atoms)**	**σ^2 (Å)**	**ΔE_0 (eV)**
Cu-C/N	1.96 ± 0.03	3	0.007 ± 0.002	1.47 ± 3.75
Cu-C	2.35 ± 0.06	4	0.007 ± 0.002	1.47 ± 3.75
Cu-Cu/Rh	2.54 ± 0.03	4.5	0.009 ± 0.001	1.47 ± 3.75
Cu-C	3.15 ± 0.06	4	0.007 ± 0.001	1.47 ± 3.75

Table S5 BET surface area with pore volume and average pore diameter of catalysts **1-5**. The BET surface area is proportional to the amount of Cu in the catalyst since the catalyst with a higher amount of Cu has a larger BET surface area**.**

Catalysts	**BET surface area ($m^2 g^{-1}$)**	**Pore volume ($cm^3 g^{-1}$)**	**Average pore diameter (nm)**
1	668.8	0.399	2.38
2	692.5	0.416	2.40
3	412.7	0.263	2.55
4	258.5	0.208	3.22
5	36.5	0.038	4.21

Table S6 Best HER activity in 0.5 M H_2SO_4 solution. Overpotential of precious metal-based HER electrocatalysts @ 10 $mAcm^{-2}$ reported in the recent literature.

Catalysts	**Overpotential (mV)** @10 $mAcm^{-2}$	**Condition**	**Refs.**
$Cu/Rh(SAs)+Cu_2Rh(NPs)/G_N$	~8	H_2 saturated	this work
Commercial 20 % Pt/C	~14	H_2 saturated	this work
$Rh(SAs)\ Rh(NPs)/G_N$	92	H_2 saturated	this work
Pt-GT-1	18	-	1
Rh_xP/NPC	19	-	5
Pt1/N-C	19	H_2 saturated	6
PtRu@RFCS	19.7	N_2 saturated	7
RhP_x@NPC	22	-	8
Ru@C2N	22	N_2 saturated	9
B-Rh:Fe=2:1	25	-	10
RuNP@PDA)	27.5	-	11
Hollow Rh/C Nanoparticles	~28	N_2 saturated	12
$Mo_2TiC_2T_x$-Pt_{SA}	30	-	13
Pt/OLC	38	N_2 saturated	14
5.2 wt% Rh-MoS_2	47	N_2 saturated	15
Pt/np-$Co_{0.85}Se$	55	-	16
$Au_{75}Rh_{25}$	64.1	Ar saturated	17
Rh-MoS2-4.8	67	Ar saturated	18
29.1 Rh/SiNW	70	-	19
Rh_2S_3	~92	N_2 saturated	20
Ru@CN-0.16	126	-	21

References

1. J. N. Tiwari, S. Sultan, C. W. Myung, T. Yoon, N. Li, M. Ha, A. M. Harzandi, H. J. Park, D. Y. Kim, S. S. Chandrasekaran, W. G. Lee, V. Vij, H. Kang, T. J. Shin, H. S. Shin, G. Lee, Z. Lee and K. S. Kim, *Nat. Energy*, 2018, **3**, 773-782.
2. L. Wang, W. Zhang, S. Wang, Z. Gao, Z. Luo, X. Wang, R. Zeng, A. Li, H. Li, M. Wang, X. Zheng, J. Zhu, W. Zhang, C. Ma, R. Si and J. Zeng, *Nat. Commun.*, 2016, **7**, 14036.
3. J. N. Tiwari, A. M. Harzandi, M. Ha, S. Sultan, C. W. Myung, H. J. Park, D. Y. Kim, P. Thangavel, A. N. Singh, P. Sharma, S. S. Chandrasekaran, F. Salehnia, J.-W. Jang, H. S. Shin, Z. Lee and K. S. Kim, *Adv. Energy Mater.*, 2019, **9**, 1970101.
4. Y. Li, N. Li, K. Yanagisawa, X. Ding and X. Li, *J. Mater. Chem. A*, 2014, **2**, 1484-1492.
5. Q. Qin, H. Jang, L. Chen, G. Nam, X. Liu and J. Cho, *Adv. Energy Mater.*, 2018, **8**, 1801478.
6. S. Fang, X. Zhu, X. Liu, J. Gu, W. Liu, D. Wang, W. Zhang, Y. Lin, J. Lu, S. Wei, Y. Li and T. Yao, *Nat. Commun.*, 2020, **11**, 1029.
7. K. Li, Y. Li, Y. Wang, J. Ge, C. Liu and W. Xing, *Energy Environ. Sci.*, 2018, **11**, 1232-1239.
8. J.-Q. Chi, X.-J. Zeng, X. Shang, B. Dong, Y.-M. Chai, C.-G. Liu, M. Marin and Y. Yin, *Adv. Funct. Mater.*, 2019, **29**, 1901790.
9. J. Mahmood, F. Li, S.-M. Jung, M. S. Okyay, I. Ahmad, S.-J. Kim, N. Park, H. Y. Jeong and J.-B. Baek, *Nat. Nanotechnol.*, 2017, **12**, 441-446.
10. L. Zhang, J. Lu, S. Yin, L. Luo, S. Jing, A. Brouzgou, J. Chen, P. K. Shen and P. Tsiakaras, *Appl. Catal. B*, 2018, **230**, 58-64.
11. Y. Li, L. A. Zhang, Y. Qin, F. Chu, Y. Kong, Y. Tao, Y. Li, Y. Bu, D. Ding and M. Liu, *ACS Catal.*, 2018, **8**, 5714-5720.
12. J. Du, X. Wang, C. Li, X.-Y. Liu, L. Gu and H.-P. Liang, *Electrochim. Acta*, 2018, **282**, 853-859.
13. J. Zhang, Y. Zhao, X. Guo, C. Chen, C.-L. Dong, R.-S. Liu, C.-P. Han, Y. Li, Y. Gogotsi and G. Wang, *Nat. Catal.*, 2018, **1**, 985-992.
14. D. Liu, X. Li, S. Chen, H. Yan, C. Wang, C. Wu, Y. A. Haleem, S. Duan, J. Lu, B. Ge, P. M. Ajayan, Y. Luo, J. Jiang and L. Song, *Nat. Energy*, 2019, **4**, 512-518.
15. Y. Cheng, S. Lu, F. Liao, L. Liu, Y. Li and M. Shao, *Adv. Funct. Mater.*, 2017, **27**, 1700359.
16. K. Jiang, B. Liu, M. Luo, S. Ning, M. Peng, Y. Zhao, Y.-R. Lu, T.-S. Chan, F. M. F. de Groot and Y. Tan, *Nat. Commun.*, 2019, **10**, 1743.
17. T. Bian, B. Xiao, B. Sun, L. Huang, S. Su, Y. Jiang, J. Xiao, A. Yuan, H. Zhang and D. Yang, *Appl. Catal. B*, 2020, **263**, 118255.
18. X. Meng, C. Ma, L. Jiang, R. Si, X. Meng, Y. Tu, L. Yu, X. Bao and D. Deng, *Angew. Chem. Int. Ed.*, 2020, **59**, 10502-10507.
19. L. Zhu, H. Lin, Y. Li, F. Liao, Y. Lifshitz, M. Sheng, S.-T. Lee and M. Shao, *Nat. Commun.*, 2016, **7**, 12272.
20. D. Yoon, B. Seo, J. Lee, K. S. Nam, B. Kim, S. Park, H. Baik, S. Hoon Joo and K. Lee, *Energy Environ. Sci.*, 2016, **9**, 850-856.
21. J. Wang, Z. Wei, S. Mao, H. Li and Y. Wang, *Energy Environ. Sci.*, 2018, **11**, 800-806.